Remarks / bin size	Time lag	Fit range
1 day	-0.5 +- 0.39 days	+- 2 days
0.5 day	-0.45 +- 0.15 days	+- 2 days
0.25 day	-0.21 +- 0.15 days	+- 2 days
0.2 day	-0.35 +- 0.15 days	+- 2 days
0.1 day	-0.25 +- 0.1 days	+- 2 days
1 hour	-0.41 +- 0.04 days	+- 2 days
0.5 hour	-0.5 +- 0.04 days	+- 2 days
no bin / interpolation	-0.38 +- 0.07 days	+- 2 days
jacuzzi / 1 hour bin	-0.36 +- 0.1 days	+- 2 days
jacuzzi / interpolation	-0.45 +- 0.078 days	+- 2 days

Table B.4: The table below displays the fit results for different bin sizes. All measurements show a systematic time lag of x-rays of approximately 10 hours. As a crosscheck for the analysis program also the lightcurve of 'jacuzzi', a completely different lightcurve program, written by Daniel Kranich in Munich, was taken to calculate the correlation. It shows the same result. To crosscheck that the effect is not an artifact of binning the correlation was also calculated without binning but by interpolating between neighbouring CT1 measurements.

The analysis is based on the idea that the x-ray flares consist of ***two components***: a ***slow flare*** background component and a ***fast flare*** component which is faster than 0.5 days. The objective in this case is to determine whether TeV flares ***are correlated to the total x-ray*** flux or ***only to the fast flare component***. Therefore, the empirical correlation function is calculated for both the total x-ray flux and for the fast x-ray flares for which the ***slow component has been subtracted*** (see Fig. B.14). The slow component was estimated by fitting the slow flare (of approximately seven day duration) with a Gaussian distribution function.

Figures B.15 Fig. B.16 display the results. The highest correlation for both datasets, with and without background, is achieved for a ***small time lag of a few hours*** (gamma-rays arrive earlier). The effect has only one sigma and is not ***significant.***

The correlation ***increases*** from 0.63 +- 0.18 (3.5 σ) to 0.70 +- 0.16 (4.3 σ) when the slow x-ray component (i.e. the background) is subtracted. The increase is ***not significant***.

Time lag between the γ-light flux and the x-ray light flux

For systematic studies of the time lag the data from CT1 in 2001 were taken. If one looks at Fig. B.17 which used a ***binning of one 1 hour*** and displays time lags Δt of +-6 days one gains the impression that the curve is slightly shifted to the left. This would imply that ***γ-rays arrive slightly earlier than x-rays***.

To clarify the question about the time lag, a Gauss-distribution was fitted to the region around the origin of the correlation plot. First the time lag was determined for different bin widths. Figure B.18 has a bin width of one hour. The fit gives a ***time lag for the x-rays of 9.8 +- 0.9 hours***. Tab. B.4 displays the fit results for ***different bin widths***.

To cross check that this effect is ***not an artifact of binning***, the correlation was also calculated ***without binning***. Since the measurements from ASM/RXTE and CT1 do not precisely coincide, for each 90 s measurement of ASM/RXTE, the value from CT1 was ***interpolated*** between two measurements, if the points were not further apart than 2.5 hours. If there is no CT1 measurement which can be properly interpolated, the measurement is discarded. To ensure that the single correlation points are not correlated, the step size was also chosen to be 2*2.4=4.8 hours (24/5 h). Fig. B.19 shows the fit to the correlation when calculated with interpolated CT1 fluxes. The fit gives a ***time lag of 9.1 +- 1.9 hours***. The range for the fit has been chosen to be +-2 days.

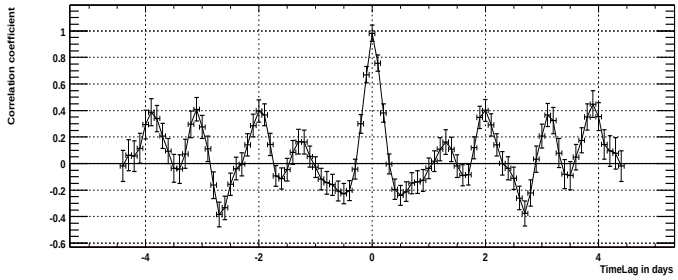

(a) ASCA Autocorrelation

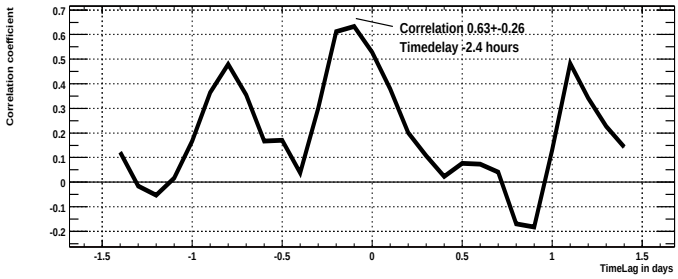

(b) Correlation with slow component

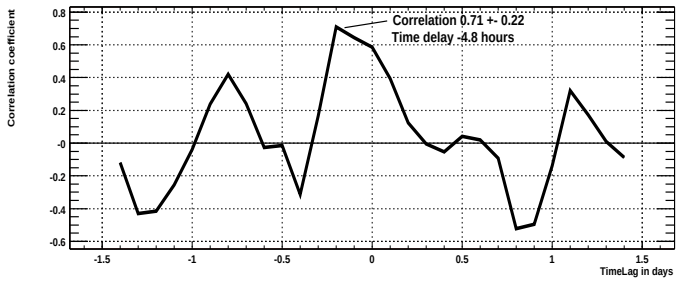

(c) Correlation subtracted slow component

Figure B.15: Plot a) shows an ASCA x-ray autocorrelation plot that illustrates the periodicities in the dataset. Plot b) shows the empirical correlation function before background subtraction which is maximally 0.63 +- 0.18. Plot c) shows the correlation function after background subtraction. It increases to 0.71 +- 0.16 which is insignificant. The two lower plots are very similar if smoothed. The plots b) and c) show a slight tendency for a time shift of a few hours.

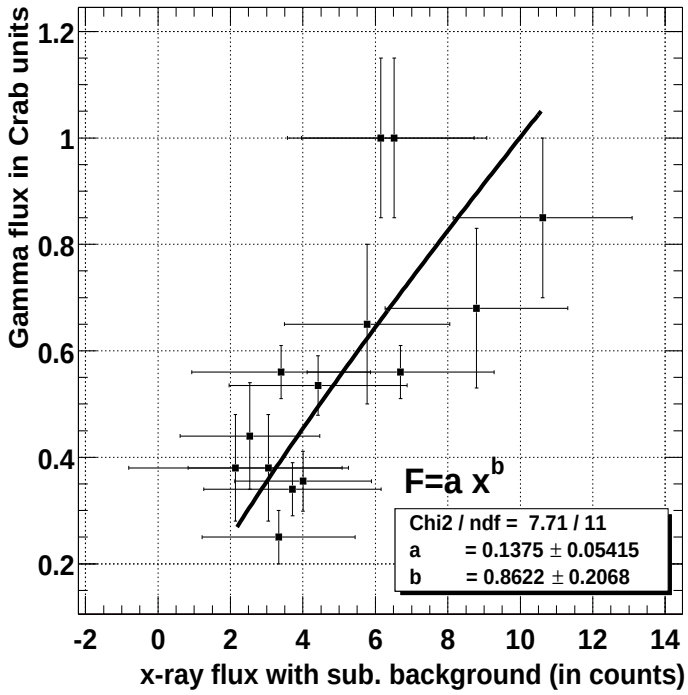

Figure B.16: This plot shows the TeV-gamma Fluxes and the x-ray fluxes plotted against each other. When subtracting the slow flare component from the total x-ray flux it was ensured that the origins of TeV flux and x-ray flux coincide. The fit of $F = ax^b$ reveals an almost perfect linear correlation between the two datasets (b=0.86+-0.2).

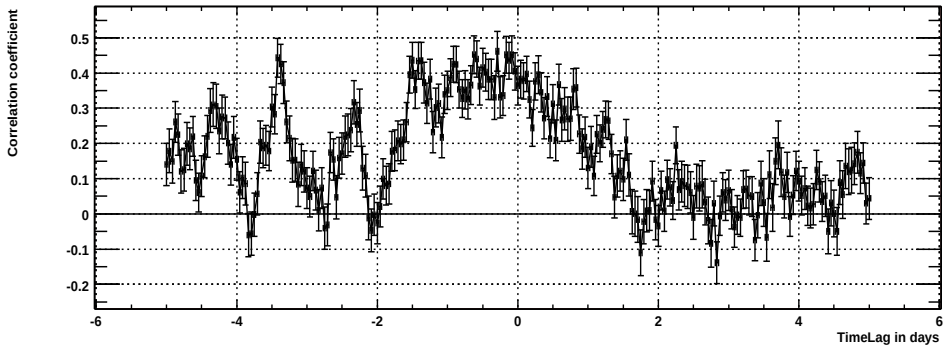

Figure B.17: In this plot with a binning of one 1 hour and time lags Δt from -6 days to +6 days one gets the impression that the curve is slightly shifted to the left. Which would mean that ***γ-rays arrive slightly earlier than x-rays.***

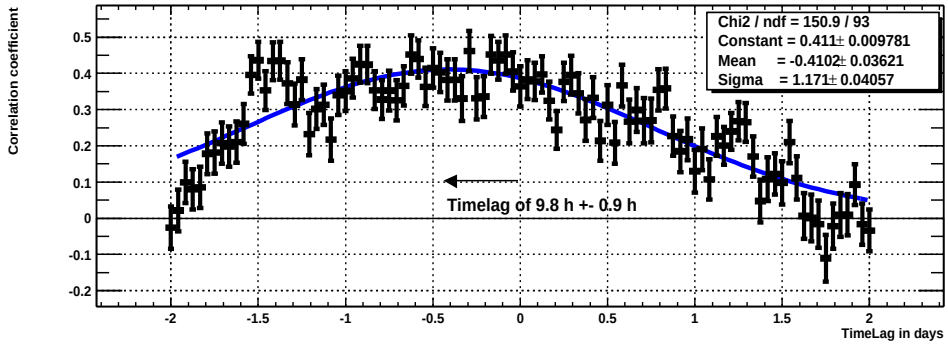

Figure B.18: In this figure only a small range (between +- 2 days) is plotted. The bin size is only 1 hour. The fit shows a time lag of 9.8 hours +- 0.9 hours.

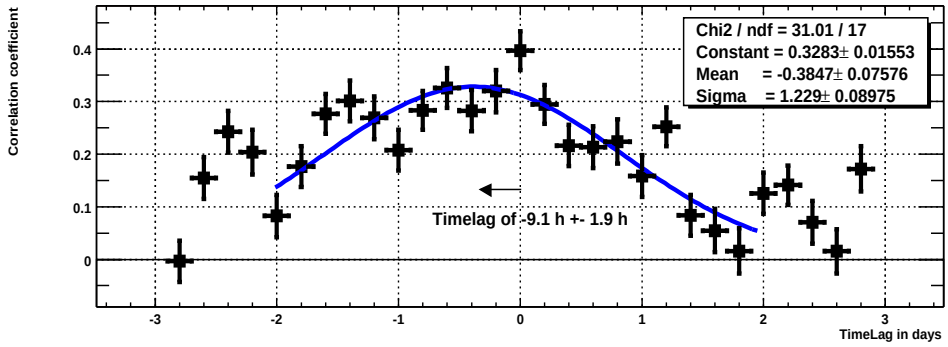

Figure B.19: In this figure the correlation was calculated without binning, but by interpolating between neighbouring CT1 measurements which are not further apart than 2.5 hours. To ensure that the data points are not correlated the step size of the time shift was chosen to be 4.8 hours (24/5 h) as well. The fit gives a time lag of 9.1 hours +- 1.9 hours.

All the measurements with different bin sizes are consistent within the errors and show a time lag of the x-rays of approximately $10 \pm 1_{stat} \pm 3_{sys}$ hours. Since the shape has large fluctuations, a change in the fit range alters the fitted time lag considerably. This means that this result also depends on the fit range. Therefore the ***systematic uncertainty*** is estimated to be approximately ***3 hours***. Taking this into account, the effect is not much larger than approximately three to four sigma for small bin sizes.

The data, especially that from the ASM/RXTE, is too noisy to give an answer of greater precision. Yet, it can be stated that in all of the plots, without exception, a ***systematic shift*** to the left (γ-photons arrive a few hours earlier) has been observed. The result has been cross checked with the light curve calculated by 'jacuzzi' (written by Daniel Kranich in Munich), another light curve calculation program of a completely separate analysis software.

Still, it ***cannot be clarified*** whether the time lag in the discrete correlation function is due to a ***real physical time lag***. This subject will be discussed in detail in chapter 4.

B.1.5 Conclusion about the γ-ray/x-ray correlation studies

CT1-γ-flux and ASM-x-ray-flux:

It can be concluded that there is a ***significant correlation*** of 0.74 +- 0.05 (in 1 day bins) between the x-ray flux and the γ-ray flux. The correlation between these fluxes can clearly be seen even by eye in Fig. B.13. A fit of a function $F = ax^b$ shows that the ***correlation is almost linear*** (b=1.0+-0.2). The empirical correlation coefficient increases monotonically with bin size probably due to the improved statistics of the bins that are involved. It is possible that this increase with bins size has a physical reason as well***.***

The hint about a possible ***time lag*** between the x-rays and the gammas of a few hours (~$10 \pm 1_{stat} \pm 3_{syst}$ hours) is of considerable interest. This time lag has not only been observed with the CT1 lightcurve calculated by this program package in C++/ROOT, but also using the lightcurve calculated by the ***'jacuzzi'*** program written by Daniel Kranich in Munich. This proves redundancy of the lightcurve calculation. The apparent time lag of the x-rays can be also explained with an asymmetric shape of the (longer) flares. Different parameters for the rise (acceleration) and fall time (cooling) could result in such an effect.

ASCA-x-ray measurement:

The ASCA x-rays measurement from a flare of Mkn 421 in April/May 1998 is much more detailed than the ASM measurements. The x-ray flares can be ***divided into a slow flare component*** (of ~seven days duration) ***and a very fast flare component*** (shorter than 0.5 days duration). Also for the measurement from ASCA a ***clear correlation*** between x-ray flux and TeV γ-flux can be observed. It was studied whether the γ-flux is mainly correlated to the fast x-ray component or to the total x-ray flux. For both cases a rather high correlation was found. The maximum correlation for the TeV flux and the total x-ray flux is 0.63 +- 0.22. If the s***low component is subtracted*** the correlation ***increases*** to 0.71 +- 0.16 which is ***insignificant.***

The correlation between the TeV γ-flux and x-ray-flux is almost linear just as above (b=0.85 +-0.2) and, as before, a weak hint of a time lag between x-rays and γ's of approximately 4 hours was be observed.

The observed timelag:

The observed timelag of the x-rays has only an estimated significance of ***three sigma*** since the said systematical error is large. However, a potential timelag could originate from either ***opacity effects*** (x-rays escape later and γ escape immediately from the surface) or ***cooling effects*** of the VHE electrons in the jet (in the beginning many γ-rays are produced but later when the electrons cooled down they only emit x-ray-synchrotron radiation).

The timelag could even be a first sign of quantum gravity effects where theoreticians expect changes in the speed of light for photons with energies close to the Planck mass. The time lag of x-rays would point to an ***increase*** of the speed of light for increasing photon energies. Even that the energy of TeV photons is far away from the Planck scale, the long distance from Mkn 421 to earth could help to amplify even tiny effects.

Still, it ***cannot be clarified*** whether the time lag in the discrete correlation function is due to a ***real physical time lag***. The effect could also be due to a very ***asymmetric shape*** of the x-ray flares. This subject will be discussed in chapter 4.

B.1.6 The hardness ratio as measured by CT1 in 2001

The hardness ratio describes the ***steepness*** of a differential spectrum for a given source (e.g. Mkn 421) in small ***time bins*** (which correspond to single runs in our case). It is calculated together with the lightcurve as was described in detail earlier. Its ***advantage*** over a spectrum is that it ***needs less statistics*** and can be calculated for single runs. The hardness ratio gives us the ***possibility*** to see whether the spectral index of the power law spectrum ***changes*** during different flare states. Figures B.20, B.21 and B.22 show the hardness ratio for different energy intervals as a function of the total flux.

The hardness ratio is the ratio of the integrated flux of a higher energy interval and that of a lower energy interval. For an assumed power law spectra, $\frac{dF(t')}{dE} = F_0\,(t)\,E^{-\alpha}$, there is a clear relation between the hardness ratio and the spectral index. The hardness ratio for a time bin i and the energy intervals $[E_{upper,min}, E_{upper,max}]$ and $[E_{lower,min}, E_{lower,max}]$ is given by:

$$H\,(t_i) = \frac{\int_{t_{min,i}}^{t_{max,i}} dt' \int_{E_{upper,min}}^{E_{upper,max}} dE\, \frac{dF(t')}{dE}}{\int_{t_{min,i}}^{t_{max,i}} dt' \int_{E_{lower,min}}^{E_{lower,max}} dE\, \frac{dF(t')}{dE}} \tag{B.4}$$

$$= \frac{\frac{F_{0,i}\left[E^{-\alpha_i+1}\right]_{E_{upper,min}}^{E_{upper,max}}}{-\alpha_i+1}}{\frac{F_{0,i}\left[E^{-\alpha_i+1}\right]_{E_{lower,min}}^{E_{lower,max}}}{-\alpha_i+1}}$$

$$H\,(t_i) = \frac{E_{upper,max}^{-\alpha_i+1} - E_{upper,min}^{-\alpha_i+1}}{E_{lower,max}^{-\alpha_i+1} - E_{lower,min}^{-\alpha_i+1}} \tag{B.5}$$

For a given hardness ratio the differential spectral index α_i can be obtained numerically.

To detect a change in the hardness ratio as a function of the flux in the data of the very fast flaring source Mkn 421 the following procedure was applied.

First the fluxes in the lower and upper energy interval were calculated for each run. Unfortunately the statistics of a single 20 minute run does not contain enough statistical information to calculate the hardness within that run. To collect ***more statistics***, the measurements of the fluxes in the low energy interval and the high energy interval were ***re-binned*** into total flux bins (consisting of approximately 10 bins), as described in Equ. E.35 (Appendix A). Since some of the measurements had huge errors, a quality cut of $F_i > \sigma_i$ was introduced. This quality cut did not change the shape of the fit result but it did reduce the fluctuations in the re-bins significantly.

Tab. B.5 ***shows the quantitative fit results*** for different energy intervals (LI=Lower energy interval, UI=upper energy interval). For each plot a constant ($y = a$, denoted as ***'CO'***) and a straight line ($y = a + mx$ denoted as ***'SL'***) were fitted and the quantity χ^2/NDF and its significance of rejection (of the constant fit only) were computed. For a straight line, the parameters (in units of hardness ratio) are 'a' (a constant) and 'm' (the slope). For a constant fit there is just the single parameter 'a'. The last two columns contain the spectral index for an assumed power law spectrum for a flux of $F = 4.0 \cdot 10^{-11} cm^{-2} s^{-1}$ and for $F = 12.0 \cdot 10^{-11} cm^{-2} s^{-1}$.

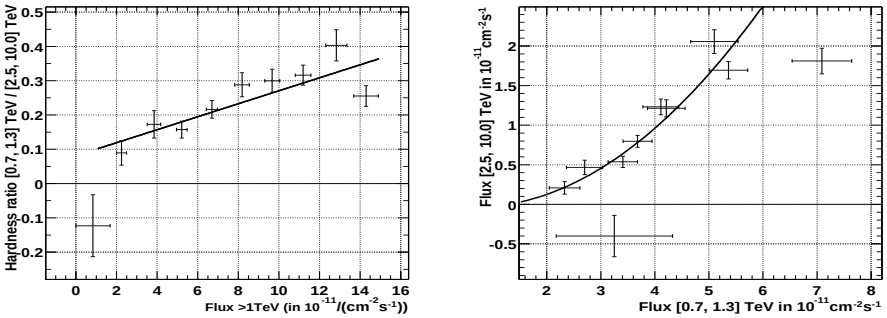

(a) (b)

Figure B.20: These plots display the hardness ratio for the intervals [0.7, 1.3] TeV and [2.5, 10.0] TeV and the correlation between the flux in the lower energy interval and the higher energy interval. a) The ***hardness ratio clearly changes with flux***. A constant fit was rejected with 4.2 sigma. In figure b) the flux in the lower energy interval [0.7, 1.3] TeV is plotted against the flux in the upper energy interval [2.5, 10.0] TeV as a cross check. This is a plot to cross check the distribution. The χ^2/NDF values are listed in Tab. B.5.

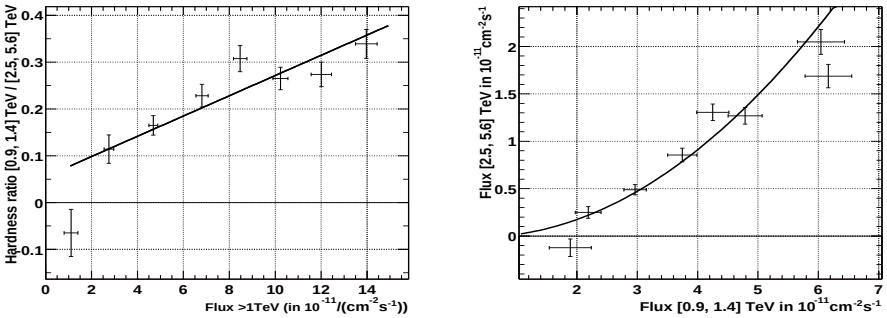

(a) (b)

Figure B.21: a) This plot displays the hardness ratio for the intervals [0.9, 1.3] TeV and [2.0, 5.6] TeV. It shows that the ***hardness ratio again increases with flux***. Although the effect is smaller than that of the previous plot, a constant fit was rejected with 3.3 sigma. In figure b) the flux in the lower energy interval ([0.9, 1.4] TeV) is again plotted against that in the upper energy interval ([2.0, 5.6] TeV), as a cross check. The χ^2/NDF values are listed in Tab. B.5.

LI/TeV	UI/TeV	Fit	$a/10^{-2}$	$m/10^{-2}$	χ^2/NDF	Sig
[0.7, 1.3]	[2.5, 10]	CO	24±4		57.3/9	4.2
[0.7, 1.3]	[2.5, 10]	SL	8.1 ± 2.7	1.9 ± 0.3	17.5/8	
[0.9, 1.4]	[2.5, 5.6]	CO	17±4		83.5/7	5.6
[0.9, 1.4]	[2.5, 5.6]	SL	5.5 ± 2.3	2.1 ± 0.3	12.6/6	
[1.0, 2.0]	[2.5, 5.6]	CO	24±3		15/9	1.2
[1.0, 2.0]	[2.5, 5.6]	SL	22 ± 2.0	0.2 ± 0.2	13.9/8	
[1.6, 2.2]	[2.5, 5.6]	CO	80±7		9.47/12	0.4
[1.6, 2.2]	[2.5, 5.6]	SL	80 ± 7.0	0 ± 1.0	9.47/11	

LI/TeV	UI/TeV	Fit	$\alpha(Flux = 4.0)$	$\alpha(Flux = 12.0)$
[0.7, 1.3]	[2.5, 10]	CO	2.5 ± 0.1	
[0.7, 1.3]	[2.5, 10]	SL	2.7 ± 0.1	2.3 ± 0.1
[0.9, 1.4]	[2.5, 5.6]	CO	2.75 ± 0.15	
[0.9, 1.4]	[2.5, 5.6]	SL	3.1 ± 0.15	2.4 ± 0.15
[1.0, 2.0]	[2.5, 5.6]	CO	2.65 ± 0.2	
[1.0, 2.0]	[2.5, 5.6]	SL	2.68 ± 0.3	2.62 ± 0.3
[1.6, 2.2]	[2.5, 5.6]	CO	2.8 ± 0.2	
[1.6, 2.2]	[2.5, 5.6]	SL	2.8 ± 0.2	2.8 ± 0.2

Table B.5: The table shows ***the quantitative fit results*** for different energy intervals (LI=Lower energy interval, UI=upper energy interval). For each plot a constant ($y = a$, denoted as ***'CO'***) and a straight line ($y = a + mx$ denoted as ***'SL'***) were fitted and the quantity χ^2/NDF and its significance of rejection (of the constant fit only) were computed. For a straight line, the parameters (in units of hardness ratio) are 'a' (a constant) and 'm' (the slope). For a constant fit there is just the single parameter 'a'. The last two columns contain the ***spectral index*** for an assumed ***power law*** spectrum for a flux of $F = 4.0 \cdot 10^{-11} cm^{-2} s^{-1}$ and for $F = 12.0 \cdot 10^{-11} cm^{-2} s^{-1}$.
It can be seen that the hardness ratio increases with increasing flux but only for the lower energy interval just above the threshold. There, the constant fit was ***rejected with 4.2 sigma***.

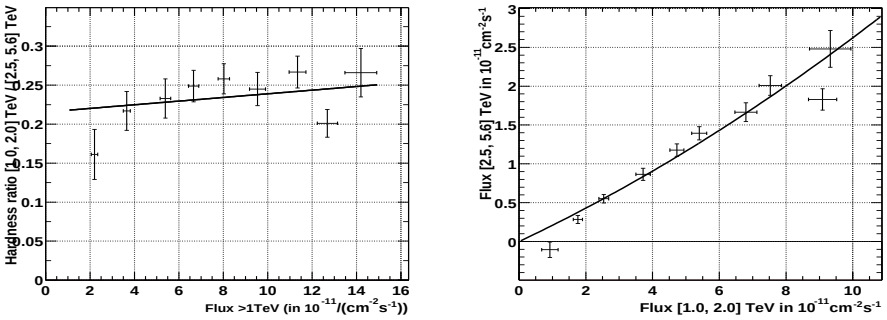

(a) (b)

Figure B.22: Plot a) shows the hardness ratio for the intervals [1.0, 2.0] TeV and [2.5, 5.6] TeV. The change in hardness ratio becomes much smaller for higher energies. In the region above 2 TeV the ***hardness ratio is almost constant*** but still displays a slight increase with increasing flux. Figure b) displays the cross check for the intervals [1.0, 2.0] TeV and [2.5, 5.6] TeV. Here the correlation plot shows almost a straight line. The hardness ratio is virtually constant. The χ^2/NDF values are listed in Tab. B.5.

It can be seen that the hardness ratio increases with increasing flux but only for the lower energy interval just above the threshold. There, the constant fit was ***rejected with 4.2 sigma.*** Lower energy intervals above 1.6 TeV show a constant hardness ratio. This will be discussed in detail in the conclusions below.

Conclusion concerning the hardness ratio calculation

In the figures above it could already been seen that ***the hardness ratio increases with increasing flux***. However, the change ***increases*** with ***decreasing*** energy. The effect is largest just above the threshold. Above 2.0 TeV the hardness ratio stays virtually constant. To determine whether this is a significant effect, potential systematic errors must be discussed carefully.

Energy intervals close to the threshold introduce large systematic errors in the calculation of the hardness because the slope of the effective detection area is very steep in those regions. However, these ***systematic errors in the calculation of the hardness are static***, they do not change with time or run. To ***exclude any bias*** from varying thresholds due to different zenith angles ***only events with zenith angles between 10° and 20°*** were considered. The threshold remains virtually unchanged in this region. Even if there are systematic errors in the flux calculation (and thus in the hardness ratio calculation), due to incorrect collection areas too close to the threshold, the effect of a ***change*** in the hardness ratio will persist.

The ***spectral indices***, obtained from the hardness ratios, ***are consistent with the spectrum*** which is presented in the following section. In general, they clearly show that the spectral index (at energies of approximately 1 TeV) is ***increasing from about*** $\alpha = 2.4$ ***up to about*** $\alpha = 3.0$ from low fluxes ($F = 4.0 \cdot 10^{-11} cm^{-2} s^{-1}$) to high fluxes ($F = 12.0 \cdot 10^{-11} cm^{-2} s^{-1}$).

How could a different hardness ratio behavior for different energy intervals be explained ? An explanation could be that the peak emission of inverse Compton scattered γ-photons is not far away from the measurement (lets say at about 10 to 100 GeV). Below 1 TeV the spectrum does not have a power-law shape anymore. It is curved there and only above 1 TeV it gets a power law shape. During flare the peak moves slightly to higher

energies. The hardness ratio only changes if parts of the lower energy interval is below approximately 1 TeV. This result will be compared with observations from the spectrum.

B.2 Spectrum of Mkn 421

The last aspect of the Mkn 421 data sample, that is going to be analyzed is the shape of the spectrum. The ***energy bin size*** (in logarithmic scale) has been chosen to be of the double size (two sigma) of the average energy resolution (~23 %).

In the second stage the spectra of different flux-states are compared to each other. As predicted by the studies of the hardness ratio a change in the slope of the spectrum at lower energies is expected.

B.2.1 The spectrum averaged over all flares

The average spectrum was calculated out of the complete dataset of the flares of Mkn 421 in 2001 (which accumulate to 259 hours of observation time).

Power law with exponential cutoff hypothesis

Figure B.23 shows the average spectrum of Mkn 421 for the period between 59125 MJD and 59250 MJD. Two differential flux $\frac{F(E)}{dE}$ functions have been fitted to the spectrum.

1. The first hypothesis is a simple ***power-law spectrum*** with spectral index α:

$$\frac{F(E)}{dE} = F_0 E^{-\alpha} \tag{B.6}$$

2. The second hypothesis is a ***power-law with an exponential cutoff*** E_c:

$$\frac{F(E)}{dE} = F_0 E^{-\alpha}\, e^{-\frac{E}{E_c}} \tag{B.7}$$

The first hypothesis of a power-law spectrum gave a spectral index of α =2.96 +- 0.04 but has been ***rejected*** with a chi-square of χ^2/NDF=74/9. This has a probability of p=10^{-21} or 6.6 sigma (Gaussian normal distribution).

The spectrum has been fitted with a power law having an exponential cutoff (upper plot). The ***spectral index is*** α ***=1.88 +- 0.15*** and the ***cutoff is located at*** E_c ***=3.1 +- 0.5 TeV***. The points with ***different colors represent 6 different zenith angle bins*** ranging up to 50°. The ***black points*** are data from ***all zenith angles*** combined. In the lower left hand plot the expected excess event distribution for a power law with cutoff has been fitted to the experimental excess event distribution. The ***fit to the excess event distribution*** is expected to yield the preciser results because the unfolding procedure introduces additional errors. The spectral index found here is α ***=2.1 +- 0.07 with a cutoff of*** E_c ***=3.1 +- 0.26 TeV*** and is therefore perfectly consistent with the upper plot. The plots for the background estimation for each (unfolded) energy bin can be found in ***Appendix B***. The background for the measurement at 12 TeV was difficult to estimate and could have a higher systematic uncertainty.

The systematic uncertainties, as already discussed in the last chapter, have their origin mainly in imperfect calibration of the absolute energy scale and in imperfect MC studies. It is estimated that the systematic uncertainty of the spectral index is $\sigma(\alpha_{sys}) = 0.1$, that of the energy cutoff is $\sigma(E_{cut}) = 1\,TeV$ and that of the flux is $\sigma(F_0) = 10\%\, F_0$.

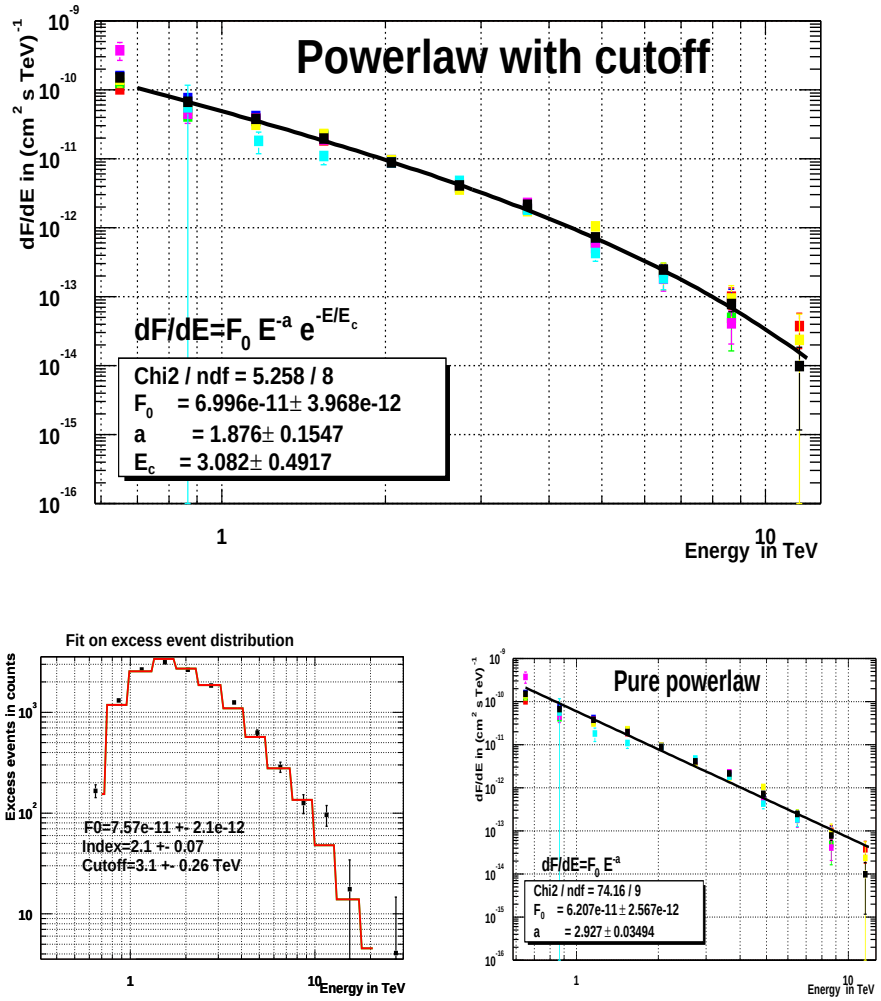

Figure B.23: Plot a) shows the average spectrum. It was fitted with a power law having a exponential cutoff. The ***spectral index is 1.88 +- 0.15*** and the ***cutoff is located at 3.1 +- 0.5 TeV.*** The points with different colors represent 6 different zenith angle bins ranging up to 50°. The black points are data from all zenith angles combined. In plot b) the expected excess event distribution for a power law with cutoff was fitted to the ***experimental excess event distribution***. This avoids the unfolding procedure and yields smaller errors for the fit parameters. The ***spectral index found here is 2.1 +- 0.07*** with a ***cutoff of 3.1 +- 0.26 TeV.*** Plot c) shows the fit of a pure power law fit which is rejected with a χ^2/NDF=74/9.

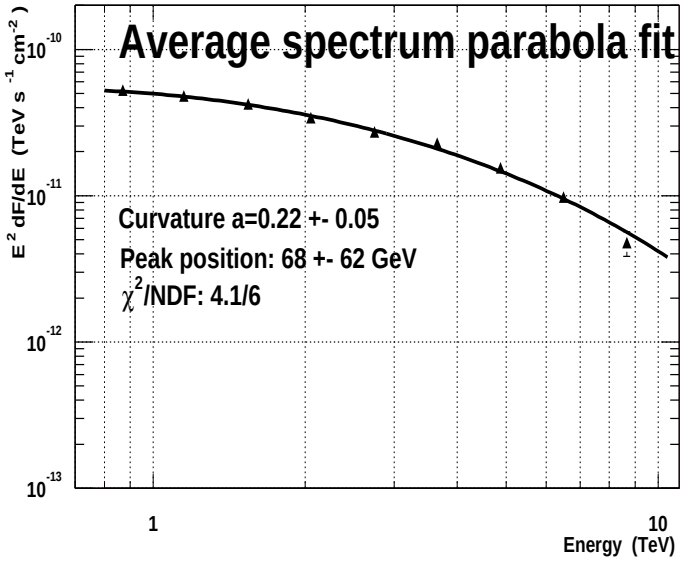

Figure B.24: The curvature in the spectrum shown here might not only originate from a cutoff, but from an intrinsic curvature of the spectrum, since what is observed, is supposed to be a portion of the inverse Compton peak. A function that is proportional to the luminosity and contains a parabolic term was fitted here: $L \propto E\frac{dF}{dE} = F_0 E^{-\alpha-\beta \ln E}$. The chisquare is χ^2/NDF=4.1/6, which is perfectly acceptable. The fit gives a value for the curvature term of a=0.22, which will be used later when the spectra of different flux states are analyzed. The spectrum was plotted in units of $E^2 dF/dE$ for better illustration.

Power law with a parabolic term

The observed curvature in the spectrum might ***not only*** originate from ***a potential cutoff*** (for example from the absorption of the cosmic infrared background) but also from an ***intrinsic curvature*** of the spectrum. What we are supposed to observe is a portion of the ***inverse Compton peak,*** which naturally posses a curvature rather than a pure power law shape. This idea will be studied further when the spectra of different flux levels are examined.

To first order the peak shape can be approximated by a ***quadratic term***. The resulting function is a parabola (in log-log scale). Usually SSC model predictions are presented in terms of ***luminosities***. For this reason the ansatz for the fit function is ***proportional to the luminosity*** $L \propto E\frac{dF}{dE}$. Naturally, the quadratic term is introduced in log-log scale and the parabola ansatz becomes:

$$E\frac{dF}{dE} = e^{-a(\ln E - \ln E_{peak})^2 + c} \quad \text{(B.8)}$$

$$= e^{c} \cdot e^{-a\ln^2 E - 2a \ln E \ln E_{peak} + -a \ln^2 E_{peak}}$$

$$= e^{c} \cdot e^{-a \ln E_{peak}} \cdot E^{+2a \ln E_{peak} - a \ln E}$$

$$= F_0 \cdot E^{-\alpha-\beta \ln E} \quad \text{(B.9)}$$

The last line shows that the ansatz is equal to a usual power law with a quadratic term β if

$$F_0 = e^{c} \cdot e^{-a \ln E_{peak}} \quad \text{(B.10)}$$

$$\alpha = 2a \ln E_{peak}$$

$$\beta = a$$

Instrument	Cangaroo	Whipple	CAT
Years	1992-1996	1995-1998	1996-2000
Range [TeV]	7-50	0.5-5	0.3-20
F_0	$2.8^{+1.9}_{-1.2}$	$3.20 \pm 0.17 \pm 0.6$	$2.2 \pm 0.05 \pm 0.6$
α	2.53 ± 0.18	$2.49 \pm 0.06 \pm 0.04$	$2.80 \pm 0.03 \pm 0.08$
Reference	[Tan98]	[Hil98]	[Mas01]

Instrument	CT-System	CT1
Years	1997-1999	2001
Range [TeV]	0.5-20	0.7-20
F_0	$2.79 \pm 0.02 \pm 0.5$	$3.0 \pm 0.33 \pm 0.5$
α	$2.59 \pm 0.03 \pm 0.05$	$2.5 \pm 0.1 \pm 0.1$
Reference	[Aha00]	[TW]

Table B.6: The table lists the actual flux measurements of the Crab nebula with different instruments.

Fig. B.24 shows that this ansatz fits quite well to the shape of the spectrum. The ***chi-square is χ^2/NDF=4.1/6***. The fit gives us a value for the ***quadratic term of a=0.22,*** which will be used later when the spectrum for different flare states is examined. The fit also provides us a value for the peak of the parabola. Since the shape of the inverse Compton peak is not known and since SSC models do not predict a parabolic inverse Compton peak, this value only provides a very rough hint of the position of the real luminosity peak.

B.2.2 The Crab nebula spectrum for consistency cross check

The Crab nebula is a pulsar that permanently feeds a shock front which produces γ-rays. The spectra of shock wave acceleration have a power law shape. It has become a standard candle or calibration light source since it emits a time constant flux with a ***power law*** spectrum, given by:

$$\frac{dF}{dE} = F_0 E^{-\alpha} \tag{B.11}$$

where α is the spectral index and F_0 is the flux constant. The spectrum of the Crab Nebula was measured by many experiments. It can be used to check if the one's own analysis is consistent with common accepted results.

Fig. B.25 shows the spectrum as recorded by CT1 during the same period as Mkn 421 in ***2001***. The spectrum is flatter (or harder) than that of Mkn 421. Since the Crab nebula is in our galaxy no absorption from the cosmic infrared background is expected. The ***spectral index, as measured in this work, is*** $\alpha = 2.5 \pm 0.1 \pm 0.1$ ***and the flux constant*** $F_0 = 3.0 \pm 0.33 \pm 0.5\, TeV^{-1} cm^{-2} s^{-1}$. The energy range is, as can be seen in the figure, 650 GeV to 15 TeV. The second figure below shows the zenith angle dependence of the flux which is negligible (as is should be). Tab. B.6 shows the results from several Cherenkov telescopes.

B.2.3 Analysis of the Mkn 421 spectrum during different flare states

Remembering the results from the analysis of the hardness ratio we expect a change of curvature in the spectrum in the region at approximately 1 TeV and eventually a slight change of the spectral index of the spectrum in dependence to different flare states.

The data has been separated in essentially ***five intervals of different fluxes*** ($[0.5, 1.0]$, $[6.0, 10]$ and $[10, 15]$ in $10^{-11} TeV^{-1} cm^{-2} s^{-1}$). For all of these flare states the spectrum has been calculated.

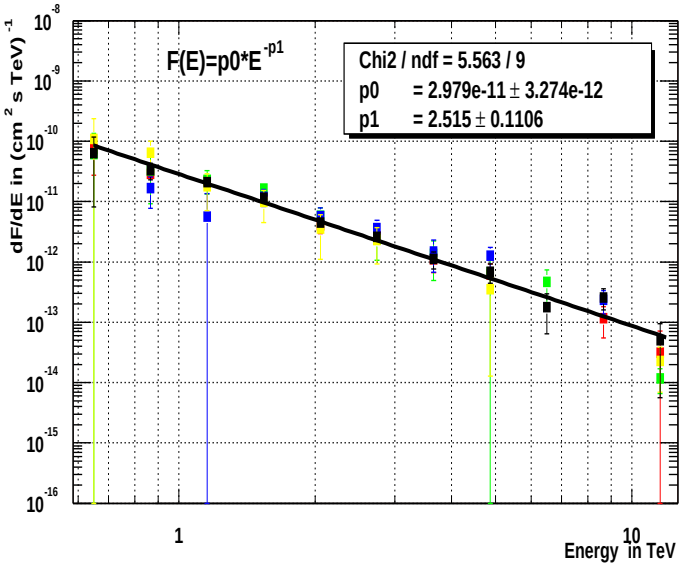

(a) Crab Spectrum

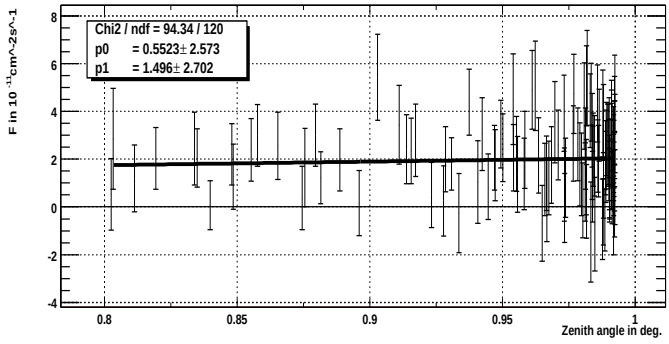

(b) Flux vs zenith angle with straight line fit

Figure B.25: The Crab nebula has become a calibration light source for Cherenkov telescopes since it emits a constant flux of γ-rays with a power law spectrum. Plot a) shows the spectrum when fitted by a power law. As usual, different colors represent different zenith angles bins and the black points are the sum of all zenith angles combined. The fit gives a ***spectral index of*** $\alpha = 2.5 \pm 0.1$ and a ***flux constant of*** $F_0 = 3.0 \pm 0.33$. b) A straight line fit ($y = p0 + p1 * x$) shows that the zenith angle dependence of the flux above 1 TeV is negligible.

$Interval$	T_{obs}	F_0	α	χ^2/NDF
in TeV	in h	$TeV^{-1}cm^{-2}s^{-1}$		Fixed cutoff, free slope
$[0.5, 1.0]$	21.7	$2.05 \pm 0.26\,10^{-11}$	2.50 ± 0.2	$1.0/4$
$[1.0, 2.5]$	82.9	$3.17 \pm 0.17\,10^{-11}$	2.22 ± 0.08	$2.3/5$
$[2.5, 4.5]$	79.8	$7.07 \pm 0.28\,10^{-11}$	2.04 ± 0.04	$3.9/5$
$[7.0, 10.0]$	23.9	$13.4 \pm 0.53\,10^{-11}$	1.88 ± 0.04	$2.8/5$
$[10.0, 15.0]$	11.8	$19.0 \pm 8.13\,10^{-11}$	1.83 ± 0.05	$5.8/5$

Table B.7: A power law with fixed cutoff of $E_c = 3.2\,TeV$ (result from overall spectrum) was fitted. For lower fluxes the spectrum becomes ***steeper.***

$Interval$	T_{obs}	F_0	χ^2/NDF
in TeV	in h	$TeV^{-1}cm^{-2}s^{-1}$	Fixed cutoff, fix slope
$[0.5, 1.0]$	21.7	$2.05 \pm 0.26\,10^{-11}$	$17.8/5$
$[1.0, 2.5]$	82.9	$3.17 \pm 0.17\,10^{-11}$	$30.7/6$
$[2.5, 4.5]$	79.8	$7.07 \pm 0.28\,10^{-11}$	$25.6/6$
$[7.0, 10.0]$	23.9	$13.4 \pm 0.53\,10^{-11}$	$4.0/6$
$[10.0, 15.0]$	11.8	$19.0 \pm 8.13\,10^{-11}$	$5.8/6$

Table B.8: A power law with fixed cutoff of $E_c = 3.2\,TeV$ and fixed slope (slope of highest flux curve) was fitted. ***The fixed slope hypothesis was rejected by χ^2/NDF=30.7/6*** (maximum value) or ***3.7 sigma.***

Power law with exponential cutoff

The first hypothesis tested is a power law with cutoff. Figure B.26 shows the $E^2 \frac{dF}{dE}$ spectra plots of these five flux intervals.
a) A power law with fixed cutoff of $E_c = 3.2\,TeV$ (result from overall spectrum) has been fitted. It was necessary to fix one parameter to reduce the errors on the fit parameters to obtain meaningful results. The spectral index of the different flare states changes considerably. ***For lower fluxes the spectrum becomes steeper***. The fit results are listed in Tab. B.7.

b) To check the significance of the change in slope during different flares ***the slope was fixed*** to $\alpha = 1.8$, that with the highest flux (green points) and the χ^2 was obtained from each fit. ***The fixed slope hypothesis was rejected by χ^2/NDF=30.7/6*** (maximum value) or ***3.7 sigma*** (for a Gaussian normal distribution). Tab. B.8 shows that none of the other four curves fit the fixed shape well.

c) In the first fit 'a)' the cutoff has been fixed and the spectral index was free. Now we check if the fit is also compatible with a ***fixed slope of*** $\alpha = -2.0$ (slope of overall, average spectrum) and a ***free cutoff***. The fit proves that the data is ***also perfectly compatible*** with a fixed slope and a free cutoff. The ***cutoff*** moves to ***higher*** energies with ***increasing*** flux. The information available is not sufficient to differentiate between the different models. Tab. B.9 lists the fit results.
d) To check the significance of the ***existence*** of a ***cutoff*** (or a curvature) a ***pure power law*** was also fitted. ***The pure power law was rejected by a chisquare of χ^2/NDF=49/5*** (maximum value).The fit results are listed in Tab. B.10. The values in the table illustrate how the spectrum ***hardens*** with increasing flux.

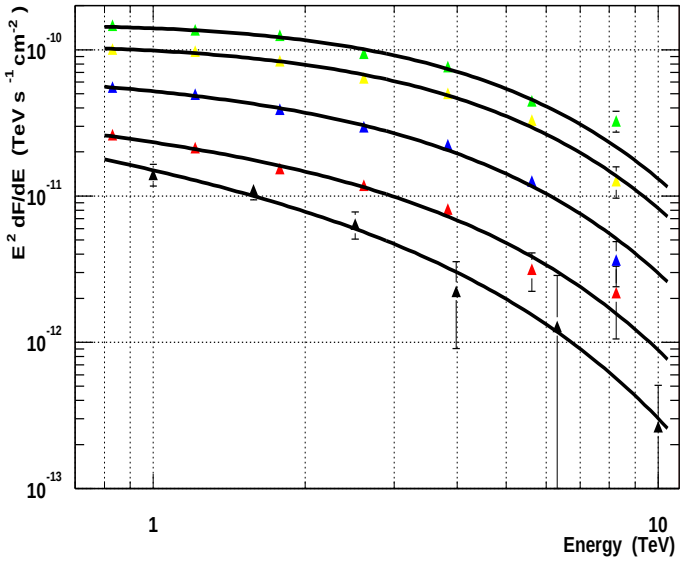

(a) Powerlaw with fix cutoff

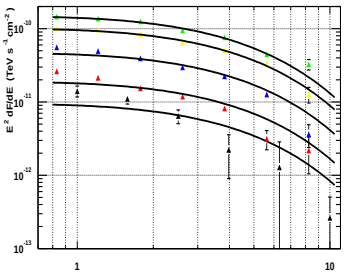

(b) Lowerlaw with fix cutoff and fix slope

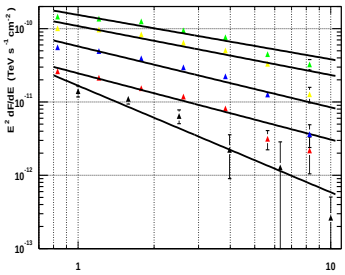

(c) Pure powerlaw fit

Figure B.26: These are $E^2 \frac{dF}{dE}$ spectra plots of various flare states. The data was separated into five intervals of different fluxes. a) The spectra for each interval was calculated and a power law with a ***fixed cutoff of*** $E_c = 3.2\,TeV$ was fitted to the data. To obtain meaningful results it was necessary to fix one parameter so that the errors on the fit parameters are reduced. The spectral index of the different flare states changes considerably. In the plot b), to check the significance of the change in slope during different flares, the slope has was to the one with the highest flux (the green points) and the χ^2 was obtained from the fits. The fixed slope was rejected by χ^2***/NDF=30.7/6*** (maximum value), or ***3.8 sigma***. c) To check the significance of the existence of a cutoff a pure power law was fitted to the data. The pure power law was rejected by χ^2***/NDF=49/5*** (maximum value).

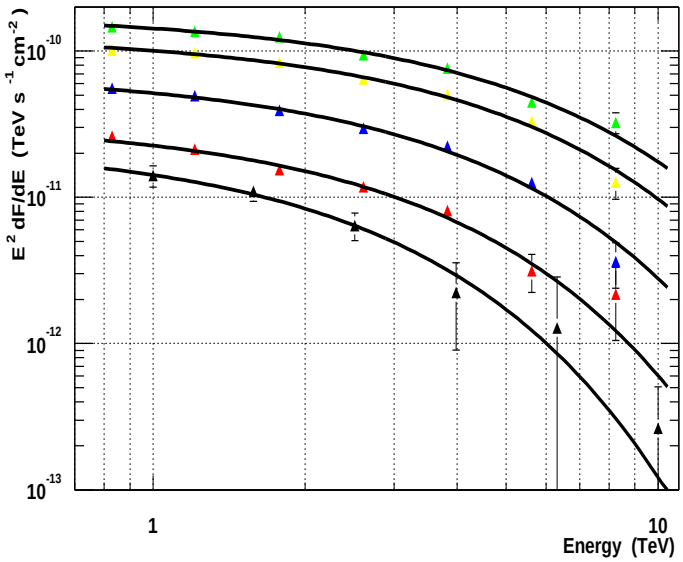

Figure B.27: This figure shows the fit of a power law with a fixed spectral index of $\alpha = -2.0$ and a free cutoff. The χ^2-values also agree to such a solution (See Tab. B.9). The cutoff moves from 1.9 TeV up to 4.3 TeV. The data is not good enough to distinguish between these different possibilities.

$Interval$	T_{obs}	F_0	Cutoff	χ^2/NDF
in TeV	in h	$TeV^{-1}cm^{-2}s^{-1}$	in TeV	Free cutoff, fixed slope
$[0.5, 1.0]$	21.7	$2.4 \pm 0.55\,10^{-11}$	1.9 ± 0.4	$0.8/4$
$[1.0, 2.5]$	82.9	$3.4 \pm 0.27\,10^{-11}$	2.5 ± 0.23	$3.5/5$
$[2.5, 4.5]$	79.8	$7.1 \pm 0.35\,10^{-11}$	3.1 ± 0.18	$4.0/5$
$[7.0, 10.0]$	23.9	$13.0 \pm 0.60\,10^{-11}$	4.0 ± 0.25	$2.8/5$
$[10.0, 15.0]$	11.8	$18.1 \pm 0.84\,10^{-11}$	4.3 ± 0.3	$3.4/5$

Table B.9: Here the ***slope was fixed*** and ***cutoff was kept free***. As expected the cutoff moves to ***higher*** energies for ***increasing*** flux. The chisquare values are acceptable. The slope and the cutoff are highly correlated parameters. The information available does not permit to differentiate between different models.

$Interval$	T_{obs}	F_0	α	χ^2/NDF
in TeV	in h	$TeV^{-1}cm^{-2}s^{-1}$		Pure powerlaw
$[0.5, 1.0]$	21.7	$1.7 \pm 0.19\,10^{-11}$	3.50 ± 0.14	$7.4/4$
$[1.0, 2.5]$	82.9	$2.5 \pm 0.12\,10^{-11}$	2.90 ± 0.06	$11.6/5$
$[2.5, 4.5]$	79.8	$5.8 \pm 0.20\,10^{-11}$	2.83 ± 0.04	$49.0/5$
$[7.0, 10.0]$	23.9	$10.9 \pm 0.37\,10^{-11}$	2.66 ± 0.04	$42.5/5$
$[10.0, 15.0]$	11.8	$15.5 \pm 0.58\,10^{-11}$	2.6 ± 0.04	$23.4/5$

Table B.10: To check the significance of the ***existence*** of a ***cutoff*** (or a curvature) also a ***pure power law*** was also fitted. ***The pure power law was rejected by a chisquare of χ^2/NDF=49/5.***

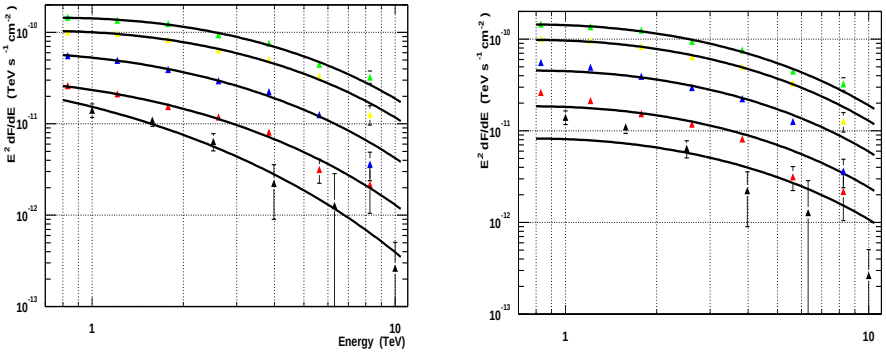

Figure B.28: A ***power law with a quadratic term*** describes the curvature of the spectrum very well. In plot a) Each spectrum has been fitted with a fixed curvature of a=0.22. This value was measured previously from the overall spectrum. From the fit the peak position of the parabola was calculated. ***It moves significantly from 13 GeV to 78 GeV***. Plot b): The peak position was fixed to E_{peak}=78.8 GeV in order to check the significance of the movement. It is evident that the resulting curves do not describe the shape of the lower flux spectra. The fits are ***rejected*** with a chisquare of χ^2***/NDF= 33/6*** (maximum value). This corresponds to a probability of $5\,10^{-8}$.

Power law with a quadratic (parabolic) term

As already mentioned, the curvature of the spectrum can also be explained also by the fact that one observes a part of the inverse Compton peak. Therefore, it makes sense to perform a fit using a ***power law with a quadratic curvature term***. This means that the inverse Compton peak is approximated by a parabola. SSC models normally give predictions about ***luminosities***. Our ansatz for the fit function is

$$L \propto E\frac{dF}{dE} = I_0 E^{-\alpha-\beta \ln E}$$

where β is the ***curvature***, α is ***spectral index*** and I_0 is the ***peak intensity*** (flux times energy). Using Equ. B.10, the ***peak position of the parabola*** can be calculated. It must be kept in mind that this value is ***not the position of the luminosity peak*** but rather a ***very rough estimate*** since the inverse Compton peak does ***not*** have a parabolic shape! Fig. B.28 shows the spectra for the five different flux intervals to which a power law with quadratic a curvature term was fitted.

What we want to test is whether the change in spectral index (or equivalent the cutoff), can be explained by the ***idea of a moving peak***. The curvature was fixed to a value of ***a=0.22*** as previously measured from the overall spectrum. The hypothesis is that the peak ***only moves*** with increasing fluxes but does ***not change its shape***. The fixing of a is also necessary to limit the number of free fit parameters to two (just as was done for the cutoff fit). This reduces the errors on the fit parameters sufficiently to obtain meaningful results.

The fit results show that the ***peak of the parabola moves from 13 GeV to 78 GeV***. The value for the intensity I_0, which is proportional to the ***peak*** luminosity suggests that the ***luminosity at peak does not change very much***. This simple model seems to show that the increase in flux (in the TeV) is mainly caused by a ***shift*** of the peak! Tab. B.11 lists the exact numbers.

To check the significance of the movement, the peak position has been fixed to E_{peak}=78.8 GeV. The fits are ***rejected with a chisquare of*** χ^2***/NDF of 33/6*** (maximum value). This corresponds to a probability of $5\,10^{-8}$ (or 3.8 sigma). This means that the change in spectral index is indeed compatible with the idea of a moving peak, even if we are not able to

$Interval$	T_{obs}	F_0	Peak	χ^2/NDF
in TeV	in h	$cm^{-2}s-1$	GeV	
$[0.5, 1.0]$	21.7	$7.2 \pm 6.1\, 10^{-10}$	13.2 ± 5.7	$1.5/4$
$[1.0, 2.5]$	82.9	$2.9 \pm 0.9\, 10^{-10}$	30.5 ± 5.7	$2.8/5$
$[2.5, 4.5]$	79.8	$4.0 \pm 0.7\, 10^{-10}$	45.4 ± 5.1	$7.3/5$
$[7.0, 10.0]$	23.9	$4.7 \pm 0.7\, 10^{-10}$	68.6 ± 7.4	$3.7/5$
$[10.0, 15.0]$	11.8	$5.7 \pm 0.9\, 10^{-10}$	78.8 ± 9.25	$2.8/5$

Table B.11: The table shows the fit results of the powerlaw fit with parabolic term. The numbers show that the ***peak of the parabola moves*** from ***13 GeV to 78 GeV*** and that the ***increase*** in flux (in the TeV) might be mainly caused by a ***shift*** of the peak rather than by an increase of the ***peak luminosity.***

$Interval$	T_{obs}	χ^2/NDF
in TeV	in h	Fix curvature a, fix peak at 78.8 GeV
$[0.5, 1.0]$	21.7	$26.2/5$
$[1.0, 2.5]$	82.9	$30.8/6$
$[2.5, 4.5]$	79.8	$33.0/6$
$[7.0, 10.0]$	23.9	$5.4/6$
$[10.0, 15.0]$	11.8	$2.8/6$

Table B.12: To check the significance of the movement, the peak position has been fixed to E_{peak}=78.8 GeV (curve with highest flux) . Three of the fits (curves with lower fluxes) are rejected significantly.

give a good estimate of the real position of the inverse Compton peak. Tab. B.12 lists the chisquare values.

B.2.4 Conclusions and a discussion of the results

Average spectrum of Mkn 421

The spectrum of Mkn 421 shows ***clear evidence*** for a cutoff at $E_c = 3.1 \pm 0.5 \pm 1\, TeV$. The pure power law was rejected at the 6.0 sigma level. The powerlaw has a spectral index of $\alpha = 2.96 \pm 0.04 \pm 0.1$. It was possible to demonstrate that a ***power law with a quadratic curvature term*** of $a = 0.22 \pm 0.05$ describes the shape of the spectrum up to 10 TeV equally well as a power law with exponential cutoff.

Spectrum of the Crab nebula

The fit of a pure power law to the spectrum of the Crab nebula gives a flux constant of $F_0 = 3.0 \pm 0.33 \pm 0.5\, TeV^{-1} cm^{-2} s^{-1}$ and a spectral index of $\alpha = 2.5 \pm 0.1 \pm 0.1$ which is in good agreement with current measurements of other experiments.

Spectra of Mkn 421 during different flare states

The spectra of different fluxes show a ***significant hardening with increasing fluxes***, which is in agreement with the results from the hardness ratio measurement. The decrease of the spectral index with increasing flux was shown by fitting a power law with fixed cutoff (at $E_c = 3.2\, TeV$). A fit with a fixed spectral index was rejected at the 3.7 sigma level.

The fit of a power law with ***fixed spectral index*** and ***free cutoff*** also gives acceptable χ^2-values. The cutoff moves from 1.9 TeV up to 4.3 TeV.

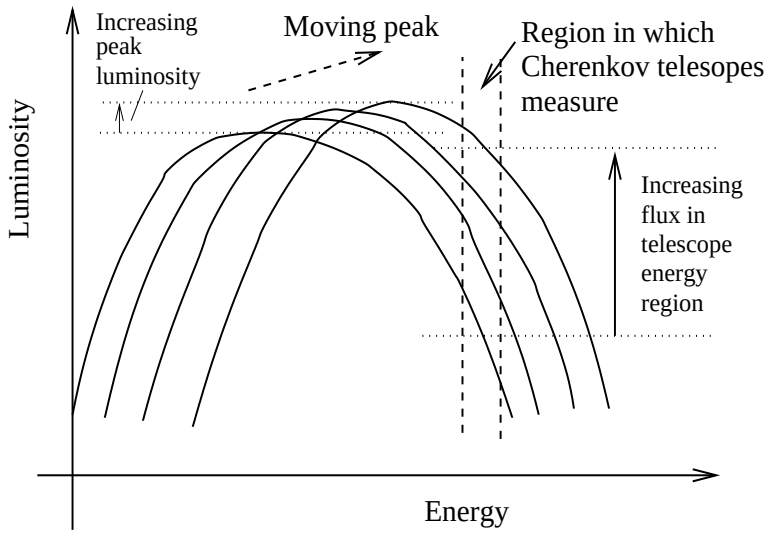

Figure B.29: The figure illustrates the model of the moving peak. The fit of a parabola to the spectra seems to show that a good part of the ***high variability*** of the flux in the TeV range is mainly caused by a ***shift of the inverse Compton peak*** to higher energies (Fig. B.29 illustrates the hypothesis) rather than by ***a high variability of the peak luminosity.***

Mkn 421 flare spectra fit by using a powerlaw with parabolic term

By fitting a power law with a quadratic curvature term (which very roughly approximates an inverse Compton peak) it was possible to show that ***the hardening of the spectrum is compatible with the idea of an moving inverse Compton peak***. The movement of the peak luminosity of the parabola from 13 GeV for low fluxes up to 78 GeV for high fluxes is significant while a ***fixed parabola peak position was rejected with 3.9 sigma***. It must be kept in mind that this rough approximation is not appropriate to estimate the real peak position of the luminosity.

The fit seems to show that a good part of the ***high variability*** of the flux in the TeV range is mainly caused by a ***shift of the inverse Compton peak*** to higher energies (Fig. B.29 illustrates the hypothesis) rather than by ***a high variability of the peak luminosity.***

Conclusion about spectra during different flare states

As a conclusion it can be noted that a ***significant*** change (a hardening for higher fluxes) in the spectrum for different flux levels could be detected. A fixed cutoff and fixed slope fit was rejected as well as a pure power law fit.

But it was not possible to ***differentiate*** between ***different*** models to find out whether the ***cutoff*** changes (fixed spectral index) or rather the ***spectral index*** (fixed cutoff). The hypothesis of a moving peak with a parabolic fit also gives acceptable χ^2-results. The truth might involve a combination of these effects.